

Data assimilation for fault slip monitoring and short-term prediction of slow slip events: an application to the 2010 long-term slow slip event in the Bungo Channel

Masayuki Kano¹, Yusuke Tanaka¹, Daisuke Sato², Takeshi Iinuma², and Takane Hori²

¹Tohoku University

²Japan Agency for Marine-Earth Science and Technology

December 3, 2023

Abstract

Monitoring and predicting fault slip behaviors in subduction zones are essential for understanding earthquake cycles and assessing future earthquake potential. We developed a data assimilation (DA) method for fault slip monitoring and short-term prediction of slow slip events (SSEs), which was applied to the 2010 Bungo Channel SSE in southwest Japan. The observed geodetic data were quantitatively explained using a physics-based model with DA. We investigated short-term predictability by assimilating observation data with limited periods. Without prior constraint on fault slip style, observations solely during slip acceleration predicted the occurrence of a fast slip; however, the inclusion of slip deceleration data successfully predicted a slow transient slip. With prior constraint to exclude unstable slip, the assimilation of data after the SSE occurrence predicted a slow transient slip. This study provided a tool using DA for fault slip monitoring and prediction based on real observation data.

Hosted file

978782_0_art_file_11637767_s4vjpn.docx available at <https://authorea.com/users/539553/articles/690515-data-assimilation-for-fault-slip-monitoring-and-short-term-prediction-of-slow-slip-events-an-application-to-the-2010-long-term-slow-slip-event-in-the-bungo-channel>

Hosted file

978782_0_supp_11637750_s4v44j.docx available at <https://authorea.com/users/539553/articles/690515-data-assimilation-for-fault-slip-monitoring-and-short-term-prediction-of-slow-slip-events-an-application-to-the-2010-long-term-slow-slip-event-in-the-bungo-channel>

1 **Data Assimilation for Fault Slip Monitoring and Short-Term Prediction of Slow**
2 **Slip Events: Application to the 2010 Long-Term Slow Slip Event in the Bungo**
3 **Channel, Japan**

4 **Masayuki Kano**^{1,2} (ORCID: 0000-0002-7288-4760),

5 **Yusuke Tanaka**¹ (ORCID: 0000-0003-4907-4919),

6 **Daisuke Sato**² (ORCID: 0000-0001-8809-9268),

7 **Takeshi Iinuma**² (ORCID: 0000-0003-0386-2055), and

8 **Takane Hori**² (ORCID: 0000-0003-3769-3894)

9 MK: Conceptualization, Methodology, Formal analysis, Funding acquisition, Writing—
10 original draft, review & editing

11 YT: Data curation, Writing—review & editing

12 DS: Supervision, Writing—review & editing

13 TI: Supervision, Writing—review & editing

14 TH: Supervision, Writing—review & editing

15 ¹Graduate School of Science, Tohoku University, Sendai, Japan.

16 ²Japan Agency for Marine-Earth Science and Technology, Yokohama, Japan.

17 Corresponding author: M. Kano (masayuki.kano.a3@tohoku.ac.jp)

18

19

20

21 **Key Points:**

- 22 • We developed a data assimilation (DA) method for fault slip monitoring and short-
23 term prediction of slow slip events (SSEs)
- 24 • Crustal deformation observed during the 2010 Bungo Channel SSE was quantitatively
25 reproduced through DA
- 26 • Observations of slow nucleation were not enough to predict evolution to an SSE or
27 earthquake without prior information on slip style

28 Abstract

29 Monitoring and predicting fault slip behaviors in subduction zones are essential for
30 understanding earthquake cycles and assessing future earthquake potential. We developed a
31 data assimilation (DA) method for fault slip monitoring and short-term prediction of slow slip
32 events (SSEs), which was applied to the 2010 Bungo Channel SSE in southwest Japan. The
33 observed geodetic data were quantitatively explained using a physics-based model with DA.
34 We investigated short-term predictability by assimilating observation data with limited
35 periods. Without prior constraint on fault slip style, observations solely during slip
36 acceleration predicted the occurrence of a fast slip; however, the inclusion of slip deceleration
37 data successfully predicted a slow transient slip. With prior constraint to exclude unstable slip,
38 the assimilation of data after the SSE occurrence predicted a slow transient slip. This study
39 provided a tool using DA for fault slip monitoring and prediction based on real observation
40 data.

41

42 Plain Language Summary

43 Various fault slips ranging from fast dynamic rupture to slow steady motion have been
44 observed in subduction zones. Understanding the current slip and predicting how it will
45 evolve in the near future are essential for assessing future slip behavior including earthquakes.
46 Data assimilation (DA) combines physics-based models and observations and is widely used
47 in weather forecasting. We developed a DA method for monitoring and predicting the fault
48 slip of slow slip events (SSEs) and applied it to real observations for the first time. The target
49 SSE was the 2010 Bungo Channel SSE in southwest Japan, where SSEs were observed at
50 recurrence intervals of approximately six to seven years. We demonstrated that DA can
51 reproduce observed crustal deformation during the SSE. Additionally, we examined short-

52 term predictability by assuming a scenario in which we acquire data for an ongoing SSE.
53 Without the knowledge of the fault slip style, the observations of slow fault acceleration were
54 not enough to predict whether it will evolve to a slow transient slip or fast dynamic rupture;
55 therefore, the accumulation of data helped in constraining the possible scenarios for future
56 slip evolution. Our study provides a basis for monitoring fault slips and their short-term
57 prediction using DA.

58

59 **Keywords**

60 Slow slip event, Data assimilation, Global Navigation Satellite System, Bungo Channel,
61 Frictional parameter

62

63 **1 Introduction**

64 Monitoring fault slip behaviors in subduction zones and predicting their short-term
65 evolution are critical for understanding seismic cycles. Specifically, we define the term
66 “monitoring” as estimating the spatio-temporal evolution of fault slips based on various
67 observation data and “prediction” as using physics-based numerical simulations to assess
68 how current slip behaviors might evolve in the imminent future through. One direct approach
69 to address both tasks is to employ data assimilation (DA) techniques (e.g., Fletcher, 2022;
70 Lewis et al., 2006). DA combines observation data with numerical models to obtain a more
71 realistic model that quantitatively explains the observations. DA is widely used in
72 meteorology and oceanology, particularly in practical applications such as weather
73 forecasting.

74 DA have been adopted for fault slip estimations in plate subduction zones (Fukuda et
75 al., 2009; Kano et al., 2020; van Dinther et al., 2019). Most previous studies have focused on
76 the optimization problem of frictional properties, which determine the fault slip behavior in
77 the physics-based model, and/or the initial values of simulation variables such as slip
78 velocities on the fault. Through optimization, observation data were quantitatively explained
79 by physics-based models. Various DA methods have been applied to the fault slip problem,
80 including the Markov chain Monte Carlo (MCMC) method (Fukuda et al., 2009), particle
81 filter (Hori et al., 2014; Mitsui et al., 2010), ensemble Kalman filter (EnKF) (Diab-Montero
82 et al., 2023; Hirahara & Nishikiori, 2019; van Dinther et al., 2019) and adjoint method (Kano
83 et al. 2013). Most of these previous studies have validated their proposed method through
84 numerical experiments using synthetic observations, with only a few studies utilizing real
85 observations.

86 DA employing real observations was successfully applied to the afterslip that
87 followed the 2003 magnitude 8.0 Tokachi-oki earthquake that occurred off the Tokachi

88 region, northeast Japan. Fukuda et al. (2009) applied the MCMC method to successfully
89 estimate the posterior probability density functions (PDFs) of frictional parameters, using a
90 single spring-slider system with a sub-daily Global Navigation Satellite System (GNSS) time
91 series for 5 h following the mainshock. Kano et al. (2015, 2020) developed the adjoint DA
92 method to optimize spatially variable frictional parameters and/or initial slip velocities from
93 daily GNSS data for 15 days following the mainshock and examined the short-term
94 predictability of afterslip for another 15 days by comparing the misfit between the observed
95 and numerically predicted crustal deformations.

96 Slow slip events (SSEs) are another research target of DA (Diab-Montero et al., 2023;
97 Hirahara & Nishikiori, 2019). Many observational studies have inferred that SSEs occurred
98 prior to megathrust earthquakes (e.g., Ito et al., 2013; Radiguet et al., 2016; Ruiz et al., 2014;
99 Voss et al., 2018), and therefore, monitoring and predicting the spatio-temporal evolution of
100 SSEs are important, particularly for assessing future earthquake potential. Hirahara and
101 Nishikiori (2019) (hereafter referred as HN19) first introduced DA to the fault slip estimation
102 problem of SSEs focusing on long-term SSEs in the Bungo Channel, southwest Japan.
103 Through numerical experiments, they demonstrated that the EnKF successfully estimated
104 frictional parameters on the fault where the SSE occurred.

105 In contrast to previous studies, to our knowledge, the present study is the first to apply
106 DA to real observations of SSEs. Assuming the fault model in HN19, we assimilate GNSS
107 data recorded during the 2010 Bungo Channel SSE using the MCMC method. Although this
108 fault model is relatively simple, we focus on how such a simple model could explain the
109 GNSS observations and predict their short-term temporal evolutions. An attempt is also made
110 to predict the temporal evolution during a single SSE, which assumes the situation that an
111 SSE is currently ongoing. We aim to evaluate the short-term evolution of fault slip. This

112 corresponds to short-term prediction of SSEs with timescales ranging from weeks to at most a
 113 few years.

114 In the remainder of this paper, we first briefly describe the DA settings. We then
 115 present the monitoring and prediction results for the 2010 Bungo Channel SSE. Finally, we
 116 discuss the predictability of the SSE's short-term evolution. Through this analysis, the present
 117 study proposes a strategy for realtime fault slip monitoring and prediction using DA.

118

119 **2 Settings of DA**

120 **2.1. Physics-based model in the Bungo Channel long-term SSE**

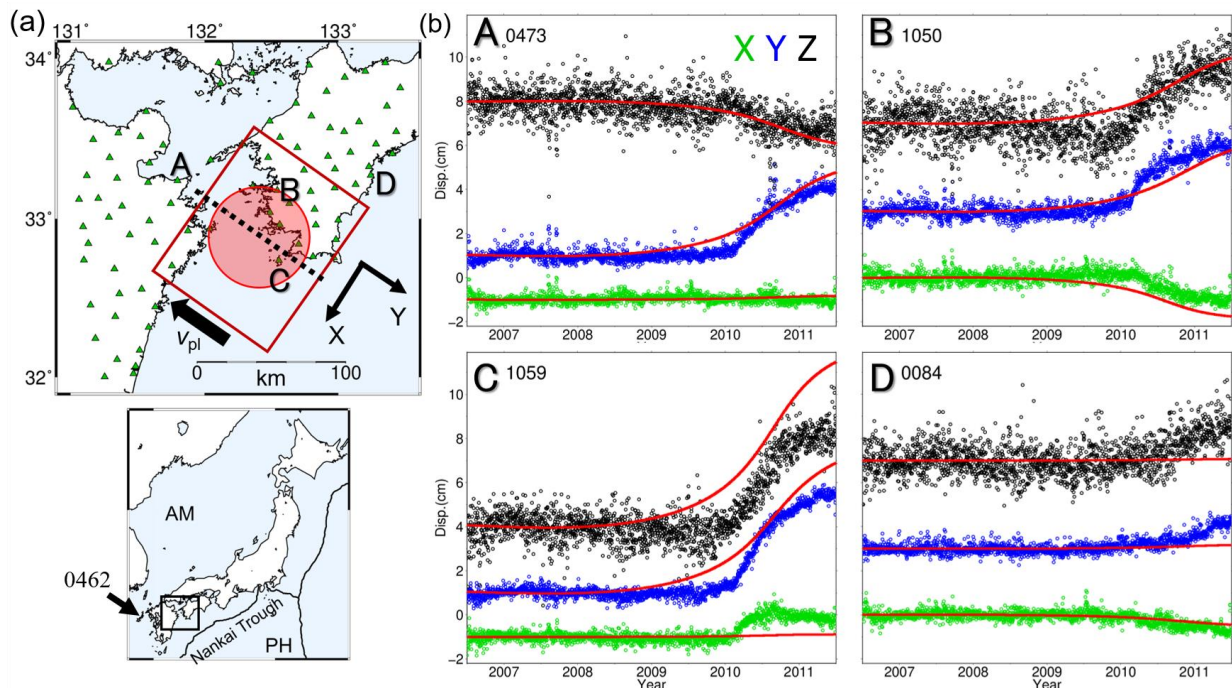
121 The Bungo Channel is located southwest of Japan in the Nankai subduction zone,
 122 where the Philippine Sea Plate subducts beneath the Amurian Plate (Figure 1a). Beneath the
 123 Bungo Channel, SSEs with a moment magnitude of ~ 7 were repeatedly observed around
 124 1980, 1985, 1991, 1997, 2003, 2010, and 2018 based on geodetic observations (Hirose et al.,
 125 1999; Kobayashi & Yamamoto 2011; Ozawa et al., 2013; Seshimo & Yoshioka 2022;
 126 Yoshioka et al., 2015). HN19 introduced a fault model that mimicked these observed
 127 characteristics of the SSEs (Figure 1a). The fault model represents a subducting plate
 128 interface as a single rectangular fault with a dip angle of 15° extending to $120 \text{ km} \times 100 \text{ km}$
 129 in the strike and dip directions, respectively. The entire fault is divided into subfaults with
 130 sizes of $2 \text{ km} \times 2 \text{ km}$; thus, the total number of subfaults is 3000. Each subfault was assumed
 131 to obey the following quasi-dynamic equation of motion (Rice, 1993):

$$132 \quad \tau_i(t) = \sum_j k_{ij} (v_{pl} t - s_j(t)) - \frac{G}{2\beta} v_i(t), \quad (1)$$

133 where the slip velocity $v_i(t)$, shear stress $\tau_i(t)$, and slip $s_i(t)$ ($=dv_i(t)/dt$) are the temporally
 134 changing simulation variables at subfault i . The second term on the right side of Equation (1)

135 represents the radiation damping (Rice, 1993) accounting for energy release owing to seismic
 136 wave radiation rather than the inertial term. The slip response function k_{ij} represents a change
 137 in shear stress at subfault i due to a unit slip at subfault j and is calculated assuming a linear
 138 isotropic elastic homogeneous half-space (Okada, 1992). The plate velocity v_{pl} , shear
 139 modulus G , and shear wave velocity β are set as 6.5 cm/yr (Miyazaki & Heki 2001), 40 GPa,
 140 and 3.0 km/s, respectively.

141



142

143 **Figure 1.** (a: top panel) The study area in southwest Japan is marked by the black rectangle in
 144 the lower image. The red square represents the Bungo Channel SSE fault region assumed by
 145 Hirahara & Nishikiori (2019). This study assumes uniform frictional parameters both inside
 146 and outside the SSE patch indicated in the red circle. The locations of GNSS stations are
 147 marked by green rectangles, with the time series for stations A–D presented in (b). The
 148 temporal slip evolution, denoted by the dotted line, is shown in Figure S2. (a: bottom panel)
 149 The tectonic setting of the study area, in which the Philippine Sea Plate (PH) subducts
 150 beneath the Amurian Plate (AM) along the Nankai Trough. (b) Examples of GNSS time

151 series at stations identified in (a). The displacements in trench-parallel (X), trench-
 152 perpendicular (Y), and vertical (Z) components are represented by green, blue, and black dots,
 153 respectively. The red lines depict the calculated time series, derived from 100 frictional
 154 parameters sampled from the posterior PDF of the model parameters. Note that red lines
 155 largely overlap, making it visually difficult to distinguish the 100 time series in each
 156 component.

157

158 To express the slip behavior of SSEs, HN19 set a circular patch of SSE with a radius
 159 of $R = 35$ km, whose center corresponds to the center of the entire fault at a depth of 25 km.
 160 HN19 used the rate- and state-dependent friction law with the aging state evolution law
 161 described by Equations (2) and (3) (Dieterich, 1979; Ruina, 1983):

$$162 \quad \tau_i(t) = \tau_{0i} + A_i \ln \left(\frac{v_i(t)}{v_0} \right) + B_i \ln \left(\frac{v_0 \theta_i(t)}{L_i} \right), \quad (2)$$

$$163 \quad \frac{d\theta_i(t)}{dt} = 1 - \frac{v_i(t)\theta_i(t)}{L_i}, \quad (3)$$

164 where $\theta_i(t)$ is a state variable representing the state of the sliding surface. τ_0 is the reference
 165 shear stress corresponding to shear stress τ for steady sliding at a reference velocity v_0 ;
 166 however, these reference values were not explicitly set here because we only calculate shear
 167 stress rate. The frictional parameters A_i , B_i , and L_i that characterize the fault slip behavior at
 168 subfault i were assumed to be uniform inside and outside the circular patch. HN19 set the
 169 frictional parameters as $(A-B, A, \text{ and } L) = (-50 \text{ kPa}, 100 \text{ kPa}, \text{ and } 40 \text{ mm})$ and $(70 \text{ kPa}, 100$
 170 $\text{kPa}, \text{ and } 40 \text{ mm})$ for subfaults inside and outside the SSE patch, respectively. These frictional
 171 parameters were determined based on the critical nucleation size R_c :

$$172 \quad R_c = \frac{\pi}{3} \frac{GBL}{(B-A)^2}. \quad (4)$$

173 For an isolated patch, when $R/R_c \ll 1$, the calculated fault slip becomes stable, while an
 174 unstable slip occurs when $R/R_c > 1$ for $0.5 < A/B < 1$ (Chen & Lapsuta, 2009; Hirahara &
 175 Nishikiori, 2019). HN19 set the frictional parameters corresponding to $R/R_c \sim 0.35$, such that
 176 the calculated slip behavior was similar to that of the long-term SSEs. The following
 177 calculations focus only frictional parameters inside the patch; parameters outside the patch
 178 were set to be the same as HN19 throughout the study.

179 Combining Equations (1)–(3), the temporal evolution of slip velocity $v_i(t)$ can be
 180 expressed as follows:

$$181 \quad \frac{dv_i(t)}{dt} = \frac{\sum_j k_{ij} (v_{pl} - v_j(t)) - \frac{B_i}{\theta_i(t)} \left(1 - \frac{v_i(t)\theta_i(t)}{L_i} \right)}{\frac{A_i}{v_i} + \frac{G}{2\beta}}. \quad (5)$$

182 By setting the initial conditions, we numerically solved Equations (3) and (5) to obtain the
 183 temporal evolutions of two independent simulation variables $v_i(t)$ and $\theta_i(t)$ for each subfault
 184 using the fourth-order embedded Runge–Kutta method (Press et al., 1996). Consequently,
 185 HN19 successfully reproduced the observed characteristics such as recurrence intervals,
 186 durations, and maximum slip velocity, in the long-term SSE of the Bungo Channel. Hereafter,
 187 we focus on one cycle of the long-term SSE, and define the initial time as two years prior to
 188 the SSE initiation when $d\theta/dt$ was approximately zero. We fixed the initial values of
 189 simulation variables at this initial time throughout the study.

190

191 2.2. GNSS observations

192 This study focuses on the Bungo Channel SSE that occurred from 2009 to 2011.
 193 Crustal deformations due to the SSE were monitored by the GNSS Earth Observation

194 Network System (GEONET) operated by the Geospatial Information Authority of Japan. We
195 used the daily GNSS time series from 86 GEONET stations around the Bungo Channel that
196 were used in HN19 after removing seven stations that were unavailable during the analysis
197 period (Figure 1a). The data period is from January 2006 to December 2011. The original
198 time series were preprocessed using the GipsyX-1.4 software (Bertiger et al., 2020) under the
199 precise point processing strategy with ambiguity resolution analysis. Station 0462 (Fukue)
200 was used as a reference site (Figure 1a). After preprocessing, we corrected offsets resulting
201 from antenna replacement and large earthquakes by subtracting the differences between the
202 coordinates respectively averaged for 10 days before and after the offset. We then rotated the
203 two horizontal components to the trench-parallel (X-axis) and trench-perpendicular (Y-axis)
204 components and subtracted the inter-SSE effect by fitting a linear function to the time series
205 from 2006.5 to 2008.5. The standard deviation for each time series was calculated from the
206 residuals of this linear trend fitting. Finally, we visually checked each time series to
207 determine whether they included any ambiguous change; if so, the station was not used in the
208 subsequent analysis.

209 Figure 1b shows examples of the GNSS time series, indicating that the transient signal
210 initiated in mid-2009 and continued for approximately two years. In the following analysis,
211 we first assimilated the GNSS time series of the three components between 2008.5 and
212 2011.5 for fault slip monitoring. Subsequently, to test the predictability of the short-term
213 evolution of fault slips, we changed the data period used for DA (hereafter referred to as the
214 DA period) to 0.5, 1.0, 1.5, 2.0, and 2.5 years. In these trials, the initial time of the DA period
215 was fixed to 2008.5, while the end was set to be 2009.0, 2009.5, 2010.0, 2010.5, or 2011.0,
216 respectively.

217

218 **2.3. MCMC method**

219 In this study, DA is conducted using MCMC, which is a technique to obtain a
 220 realization or sample \mathbf{m} from a target probability density function (PDF) $p(\mathbf{m})$. In our
 221 problem, the target PDF is the posterior PDF of the model parameter $p(\mathbf{m}|\mathbf{d})$, where \mathbf{m}
 222 consists of a set of three frictional parameters (A , B , and L) within the SSE patch, and \mathbf{d} is the
 223 observation vector. Therefore, we aimed not only to optimize the frictional parameters but
 224 also to evaluate their uncertainties. Using this information, the temporal evolution of fault
 225 slip can be predicted in a probabilistic manner.

226 Among the wide variety of MCMC methods, we used the Metropolis method, which
 227 is one of the well-known versatile algorithms (Metropolis et al., 1953). The posterior PDF is
 228 calculated using Bayes' theorem $p(\mathbf{m}|\mathbf{d}) = cp(\mathbf{m})p(\mathbf{d}|\mathbf{m})$, where $p(\mathbf{m})$ is a prior PDF of the
 229 model parameters, $p(\mathbf{d}|\mathbf{m})$ is a likelihood function, and c is a constant that is canceled out in
 230 the Metropolis method. We assume two types of prior information: uniform distributions for
 231 all the frictional parameters, and those with constraints of $R/R_c < 0.58$, that is, $R_c > 60$ km,
 232 and $0.5 < A/B < 1$. The latter prior PDF is introduced to avoid unstable slip and assumes that
 233 we know SSE will occur in the target area. The likelihood function $p(\mathbf{d}|\mathbf{m})$ is defined as the
 234 product of the misfits between the calculated and observed crustal deformations, scaled by
 235 the observation errors with a normalization constant c' :

$$236 \quad p(\mathbf{d}|\mathbf{m}) = c' \prod_{t=1}^N \exp\left(-\frac{1}{2}(\mathbf{H}\mathbf{s}_t - \mathbf{d}_t)^T \mathbf{R}^{-1}(\mathbf{H}\mathbf{s}_t - \mathbf{d}_t)\right), \quad (6)$$

237 where \mathbf{d}_t includes the observed cumulative displacement on day t . \mathbf{s}_t contains the fault slip for
 238 all subfaults, and \mathbf{H} is an observation matrix that converts simulation variables, or fault slip in
 239 this case, to observed quantities. Therefore, the product $\mathbf{H}\mathbf{s}_t$ corresponds to the calculated
 240 cumulative displacement. In this study, the observation matrix \mathbf{H} was calculated by assuming

241 a linear isotropic elastic homogeneous half-space (Okada, 1992). \mathbf{R}_t includes the observation
 242 errors described in the previous subsection, and N is the number of observation epochs.

243 The Metropolis method iteratively obtains the samples \mathbf{m} from the posterior PDF
 244 $p(\mathbf{m}|\mathbf{d})$ using the initial values of $\mathbf{m}^0 = (A, B, L)^T = (100 \text{ kPa}, 150 \text{ kPa}, 40 \text{ mm})^T$, which are
 245 used in HN19.

246 For $k = 0, 1, \dots, K-1$, repeat the following steps.

247 1. Propose a candidate for the next sample \mathbf{m}' based on the following proposal distribution
 248 and the current sample \mathbf{m}^k :

$$249 \quad \mathbf{m}' = \xi, \quad \xi \sim N(\mathbf{m}^k, \Sigma). \quad (7)$$

250 We assume Σ is a diagonal matrix.

251 2. Determine whether the candidate \mathbf{m}' is accepted or not with an acceptance ratio of $\min(1,$
 252 $p(\mathbf{m}'|\mathbf{d})/p(\mathbf{m}^k|\mathbf{d}))$. If the candidate is accepted, we set $\mathbf{m}^{k+1} = \mathbf{m}'$; otherwise, $\mathbf{m}^{k+1} = \mathbf{m}^k$.

253 We do not use the initial samples to remove the effect of the initial values. After this initial
 254 burn-in period, the resulting series of samples $\{\mathbf{m}^k\}$ ($k = 0, 1, \dots, K$) emulates an objective
 255 sample set drawn from a target posterior PDF $p(\mathbf{m}|\mathbf{d})$.

256 For each iteration, we ran a forward simulation with the initial simulation variables
 257 and assigned frictional parameters to obtain the calculated crustal deformation, which was
 258 then detrended using the time series for the first two years. Subsequently, we compared the
 259 calculated displacement with the observations to obtain a sample. We first repeated these
 260 procedures for $K = 10,000$ iterations for the global parameter search with a standard deviation
 261 of 5.0×10^{-1} kPa, 1.0 kPa, and 1.0×10^{-1} mm for A - B , A , and L , respectively in diagonal
 262 components of Σ . Following this, we conducted an additional 10,000 iterations with values of
 263 5.0×10^{-3} kPa, 1.0×10^{-2} kPa, and 1.0×10^{-3} mm for A - B , A , and L , respectively, for the local

264 search and obtained samples of the posterior PDF of the model parameters from the latter
265 10,000 samples.

266

267 **3 Fault Slip Monitoring Results of the 2010 Bungo SSE**

268 This section presents the results obtained by assimilating the GNSS data, including
269 the entire SSE period from 2008.5 to 2011.5. Frictional parameters within the SSE patch
270 were estimated as $A-B = -43.1$ kPa, $A = 77.5$ kPa, and $L = 45.9$ mm (Table 1 and Figure S1).
271 The uncertainty of each parameter was approximately five orders of magnitude smaller than
272 the parameter value itself. This implies that a slight change in the parameters will greatly
273 decrease the posterior PDF values, and the proposed values will rarely be accepted in the
274 MCMC. This may be due to the strong constraint of the assumed simple numerical fault
275 model, in which the location of the SSE patch is fixed, the frictional parameters are assumed
276 to be spatially uniform within the patch, and the slip direction is fixed. Future studies should
277 consider applying the method to a numerical model with a high degrees-of-freedom,
278 considering the spatial heterogeneity in frictional parameters, variable slip directions, and
279 geometry of the subducting plate interface.

280 Despite this model constraint, the calculated displacement time series using 100
281 randomly selected samples in Figure S1 explained the observed GNSS data (Figure 1b).
282 Notably, all 100 calculated time series mostly overlap; thus, Figure 1b indicates the small
283 uncertainty of the calculated displacement, reflecting the small uncertainty of the parameters.
284 Fault slips along the plate interface slowly accelerated in 2009 and lasted for ~2 years with a
285 maximum slip rate of $\log(V/V_{pl}) \sim 0.55$ (~11 cm/yr) (Figure S2). These characteristics are
286 roughly consistent with the kinematic inversion results of Yoshioka et al. (2015),
287 demonstrating the reproducibility of the observed crustal deformation by DA.

288

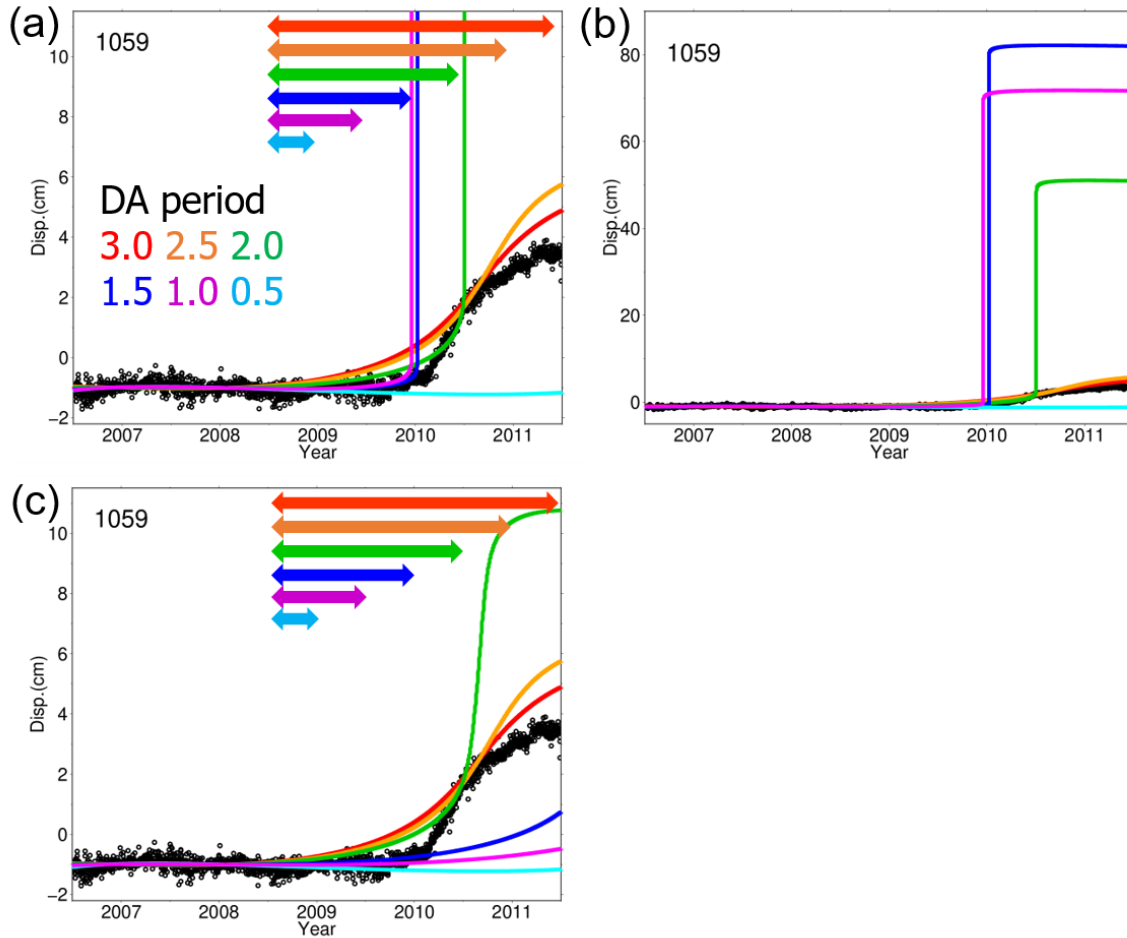
289 **4 Short-Term Prediction of Slip Evolutions of Ongoing SSE**

290 We next investigated the short-term predictability of ongoing SSE by changing the
291 DA period. This setting assumes that if we observe the currently ongoing transient signal, we
292 can predict its future evolution over subsequent days to months based on the estimated
293 frictional parameters by DA. Figures 2a, 2b and Table 1 summarize the DA and prediction
294 results and the estimated frictional parameters. Figures 2a and 2b indicate that all results
295 successfully explained the observed data during the DA period. However, the prediction
296 results showed different behaviors depending on the DA period: when we assimilated data for
297 a DA period of 2.5 years (orange line), the future evolution was predicted as a slow transient
298 slip. However, when we assimilated data for DA periods shorter than 2.0 years (green, blue,
299 and purple lines), the prediction resulted in a fast slip (Figure 2b). This implies that without
300 prior knowledge of observations showing the deceleration of a fault slip, or in other words,
301 when we only have observations during slip acceleration, the results predict the occurrence of
302 an earthquake. The estimated frictional parameters in the case of short DA periods
303 correspond to unstable slip conditions of $R/R_c > 1$ (Table 1).

304 Following these results, we conducted similar DA trials with a prior constraint on the
305 critical nucleation size R_c to avoid unstable slip. The resulting time series calculated using the
306 estimated frictional parameters (Table 1) predicted slow transient slip rather than unstable
307 slip (green, blue, and purple lines in Figure 3c). For cases with a DA period longer than 2.5
308 years, the proposed samples in the MCMC computation are not rejected by the prior
309 constraints, and therefore, the results matched those without a prior constraint on R_c .

310

311



312

313 **Figure 2.** (a) Comparison of observed (circles) and calculated (colored lines) time series
 314 without prior constraints on the critical nucleation size R_c in the trench-perpendicular
 315 component at station 1059. The calculated time series are computed using 100 frictional
 316 parameters sampled from the posterior PDF of the model parameters by assimilating the
 317 observations indicated by the corresponding colored arrows. Notably, the colored lines
 318 largely overlap, making it visually difficult to distinguish the 100 calculated time series. (b)
 319 An enlarged view of (a) in the vertical axis. (c) Same as (a) but with prior constraints on R_c .

320

321

322 **Table 1.** *Estimated frictional parameters and their uncertainties (s.d.) without and with prior*323 *constraints on critical nucleation size R_c .*

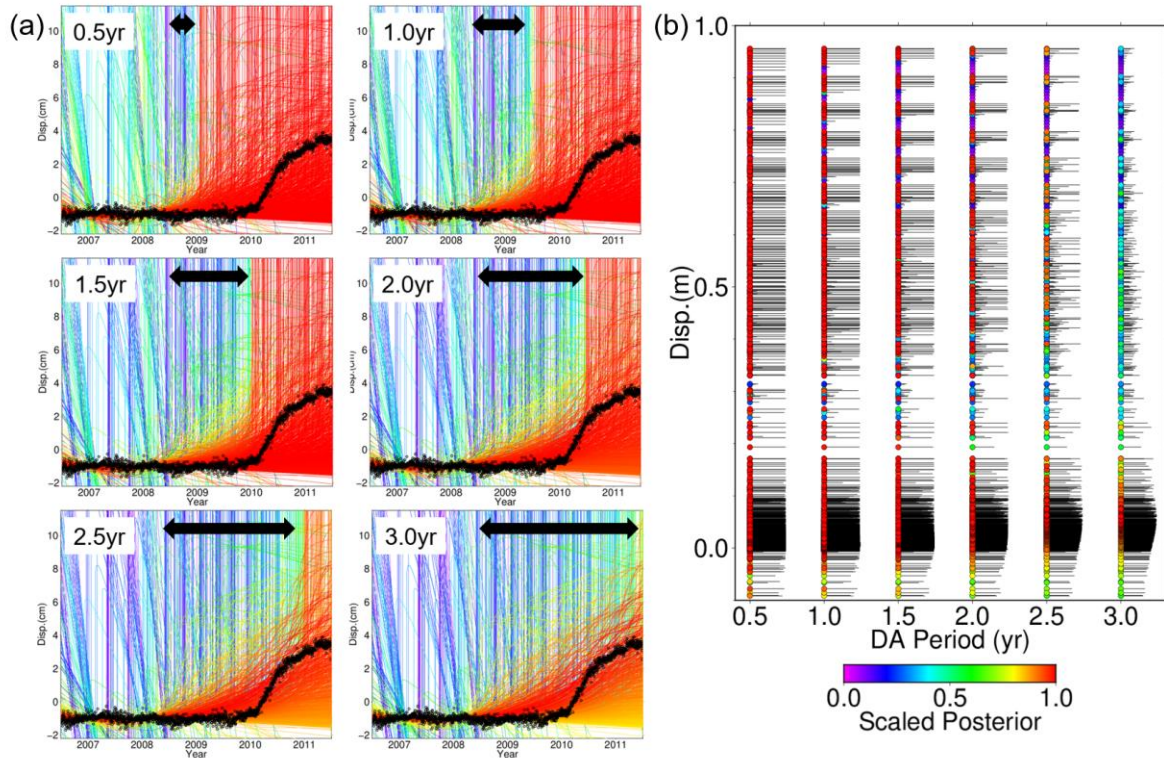
DA period	A-B (kPa) (s.d.)	A (kPa) (s.d.)	L (mm) (s.d.)	R_c (km)
Without prior constraints on critical nucleation size R_c				
0.5 yrs	-191.7 (3.2)	30.7 (4.1)	69.3 (1.1)	17.6
1.0 yr	-161.5 (8.7×10^{-2})	19.3 (1.7×10^{-1})	55.2 (8.5×10^{-3})	16.1
1.5 yrs	-180.7 (6.1×10^{-2})	39.3 (1.6×10^{-1})	46.1 (1.5×10^{-2})	13.1
2.0 yrs	-116.7 (9.4×10^{-4})	125.2 (8.9×10^{-4})	39.3 (7.7×10^{-5})	29.2
2.5 yrs*	-57.3 (3.9×10^{-4})	67.4 (4.3×10^{-4})	51.6 (1.8×10^{-4})	82.1
3.0 yrs*	-43.1 (3.1×10^{-4})	77.5 (3.8×10^{-4})	45.9 (1.3×10^{-4})	124.6
**	-50.0	100	40.0	100
With prior constraints on critical nucleation size R_c				
0.5 yrs	-137.8 (3.6)	355.6 ($1.3 \times 10^{+1}$)	71.8 (2.3)	78.2
1.0 yr	-78.2 (5.8×10^{-2})	78.3 (1.4×10^{-1})	86.0 (1.2×10^{-2})	92.2
1.5 yrs	-82.1 (4.1×10^{-2})	86.7 (1.2×10^{-1})	57.4 (1.2×10^{-2})	60.2
2.0 yrs	-71.3 (7.5×10^{-4})	105.6 (4.4×10^{-4})	41.1 (5.1×10^{-5})	60.0
2.5 yrs*	-57.3 (3.9×10^{-4})	67.4 (4.3×10^{-4})	51.6 (1.8×10^{-4})	82.1
3.0 yrs*	-43.1 (3.1×10^{-4})	77.5 (3.8×10^{-4})	45.9 (1.3×10^{-4})	124.6
**	-50.0	100	40.0	100

324 *Note.* * Same values for both results with and without prior constraints

325 **Values used in Hirahara & Nishikiori (2019).

326

327



328

329 **Figure 3.** (a) Comparison of observed (black circles) and calculated (colored lines) time series, in the trench-perpendicular component at station 1059. These calculated time series
 330 series, in the trench-perpendicular component at station 1059. These calculated time series
 331 are derived by varying a set of frictional parameters. The line colors correspond to posterior
 332 values calculated using the data in the DA period indicated by the black arrow in each
 333 subpanel. These posterior values are scaled to a range [0,1] within each subpanel. (b) Scaled
 334 posterior values as functions of the DA period in the horizontal axis and final displacement in
 335 2011.5 shown in (a) in the vertical axis. The length of each horizontal black line corresponds
 336 to the scaled posterior values.

337

338 Regardless of the prior constraint on R_c , the uncertainties in the frictional parameters
 339 decreased with increasing number of observation epochs (Table 1). This implies that the
 340 number of possible scenarios for future slip evolution decreased with data accumulation. To
 341 clarify this point, we analyzed possible scenarios for future slip evolution based on forward
 342 computations by varying the frictional parameters. We set a combination of frictional

343 parameters $A-B = -210.0-30.0$ kPa, $A = 10.0-150.0$ kPa, and $L = 30.0-100.0$ mm with
344 increments of $A-B = 10.0$ kPa, $A = 10.0$ kPa, and $L = 10.0$ mm. Thus, we conducted 1,862
345 forward computations, excluding the sets of frictional parameters with which numerical
346 integration could not be executed owing to strongly unstable behavior. In each computation,
347 the posterior values were evaluated for all DA periods. Figure 3a summarizes all calculated
348 time series or scenarios in each DA period in the Y-direction at station 1059. For trials with
349 short DA periods, the time series with high posterior PDF predicted both fast and slow slips
350 after the DA period. With long DA period, only few time series tended to predict fast slips
351 (i.e., a reduction in the number of vertical red lines), and scenarios for predicting SSEs were
352 dominant. This characteristic can be clearly observed in Figure 3b, which shows scaled
353 posterior values as functions of the DA period on the horizontal axis and the final
354 displacement in 2011.5 shown in Figure 3a. This final displacement approximately
355 corresponded to the mode of the calculated fault slips; the final displacement was large ($>$ a
356 few tens of cm) for fast slip, moderate (\sim a few to 10 cm) for slow slip, and small (~ 0 cm) for
357 stable slip. The scaled posterior values indicate that almost all the slip scenarios are possible
358 for a DA period of 0.5 years. When the DA periods became longer, the scenarios with fast
359 slips were gradually rejected. Finally, those with high scaled posterior values favor a slow
360 fault slip of ~ 6 cm in final displacement at station 1059, particularly in cases with DA periods
361 longer than 2.5 years.

362 This study assumed uniform distribution of frictional parameters as a prior PDF.
363 Bayesian estimation enables the sequential update of the prior PDF, and the posterior PDF
364 was eventually obtained after DA (Figure 3b and Table 1). The posterior PDF can be utilized
365 as prior information when conducting DA for the next SSE.

366 In summary, the observed GNSS time series were quantitatively explained by the DA,
367 independent of the DA period, even when using the simplified fault model proposed by

368 HN19. For short-term prediction, information on the deceleration of slip velocities is
369 necessary to appropriately constrain the evolution of the SSE; otherwise, the DA predicts fast
370 fault slips. Although a high degree of freedom would result in better fault slip monitoring and
371 short-term prediction with high accuracy, the present results demonstrate the effectiveness of
372 the DA for monitoring and predicting the evolution of SSEs.

373

374 **Acknowledgments**

375 This study was supported by the MEXT Project for Seismology toward Research
376 Innovation with Data of Earthquake (STAR-E) (Grant number JPJ010217), ERI JURP 2022-
377 B-06 in Earthquake Research Institute, the University of Tokyo, and JSPS KAKENHI (Grant
378 numbers JP21K03694, JP21H05206, and JP23H00466). The computer system in Earthquake
379 Research Institute, the University of Tokyo, was used in this study.

380

381 **Data Availability Statement**

382 The original GNSS data from GEONET used in this study can be downloaded from
383 https://www.gsi.go.jp/ENGLISH/geonet_english.html after registration. Figures were
384 generated using Generic Mapping Tools (Wessel et al., 2013).

385

386 **References**

387 Bertiger, W., Bar-Sever, Y., Dorsey, A., Haines, B., Harvey, N., Hemberger, D., et al. (2020).
388 GipsyX/RTGx, a new tool set for space geodetic operations and research. *Advances in*
389 *Space Research*, 66(3), 469–489. <https://doi.org/10.1016/j.asr.2020.04.015>

- 390 Chen, T., & Lapusta, N. (2009). Scaling of small repeating earthquakes explained by
391 interaction of seismic and aseismic slip in a rate and state fault model. *Journal of*
392 *Geophysical Research: Solid Earth*, *114*(B1). <https://doi.org/10.1029/2008JB005749>
- 393 Diab-Montero, H. A., Li, M., van Dinther, Y., & Vossepoel, F. C. (2023). Estimating the
394 occurrence of slow slip events and earthquakes with an ensemble Kalman filter.
395 *Geophysical Journal International*, *234*(3), 1701–1721.
396 <https://doi.org/10.1093/gji/ggad154>
- 397 Dieterich, J. H. (1979). Modeling of rock friction: 1. Experimental results and constitutive
398 equations. *Journal of Geophysical Research: Solid Earth*, *84*(B5), 2161–2168.
399 <https://doi.org/10.1029/JB084iB05p02161>
- 400 Fletcher, S. J. (2022). Data assimilation for the geosciences: From theory to application.
401 Elsevier.
- 402 Fukuda, J., Johnson, K. M., Larson, K. M., & Miyazaki, S. (2009). Fault friction parameters
403 inferred from the early stages of afterslip following the 2003 Tokachi-oki earthquake.
404 *Journal of Geophysical Research: Solid Earth*, *114*(B4).
405 <https://doi.org/10.1029/2008JB006166>
- 406 Hirahara, K., & Nishikiori, K. (2019). Estimation of frictional properties and slip evolution
407 on a long-term slow slip event fault with the ensemble Kalman filter: numerical
408 experiments. *Geophysical Journal International*, *219*(3), 2074–2096.
409 <https://doi.org/10.1093/gji/ggz415>
- 410 Hirose, H., Hirahara, K., Kimata, F., Fujii, N., & Miyazaki, S. (1999). A slow thrust slip
411 event following the two 1996 Hyuganada earthquakes beneath the Bungo Channel,
412 southwest Japan. *Geophysical Research Letters*, *26*(21), 3237–3240.
413 <https://doi.org/10.1029/1999GL010999>

- 414 Hori, T., Miyazaki, S. I., Hyodo, M., Nakata, R., & Kaneda, Y. (2014). Earthquake
415 forecasting system based on sequential data assimilation of slip on the plate boundary.
416 *Theoretical and Applied Mechanics Japan*, 62, 179–189.
417 <https://doi.org/10.11345/nctam.62.179>.
- 418 Ito, Y., Hino, R., Kido, M., Fujimoto, H., Osada, Y., Inazu, D., et al. (2013). Episodic slow
419 slip events in the Japan subduction zone before the 2011 Tohoku-Oki earthquake.
420 *Tectonophysics*, 600, 14–26. <https://doi.org/10.1016/j.tecto.2012.08.022>
- 421 Kano, M., Miyazaki, S., Ito, K., & Hirahara, K. (2013). An adjoint data assimilation method
422 for optimizing frictional parameters on the afterslip area. *Earth, Planets and Space*, 65,
423 1575–1580. <https://doi.org/10.5047/eps.2013.08.002>
- 424 Kano, M., Miyazaki, S., Ishikawa, Y., Hiyoshi, Y., Ito, K., & Hirahara, K. (2015). Real data
425 assimilation for optimization of frictional parameters and prediction of afterslip in the
426 2003 Tokachi-oki earthquake inferred from slip velocity by an adjoint method.
427 *Geophysical Journal International*, 203(1), 646–663. <https://doi.org/10.1093/gji/ggv289>
- 428 Kano, M., Miyazaki, S., Ishikawa, Y., & Hirahara, K. (2020). Adjoint-based direct data
429 assimilation of GNSS time series for optimizing frictional parameters and predicting
430 postseismic deformation following the 2003 Tokachi-oki earthquake. *Earth, Planets and*
431 *Space*, 72(1), 1–24. <https://doi.org/10.1186/s40623-020-01293-0>
- 432 Kobayashi, A., & Yamamoto, T. (2011). Repetitive long-term slow slip events beneath the
433 Bungo Channel, southwestern Japan, identified from leveling and sea level data from
434 1979 to 2008. *Journal of Geophysical Research: Solid Earth*, 116(B4).
435 <https://doi.org/10.1029/2010JB007822>
- 436 Lewis, J. M., Lakshmivarahan, S., & Dhall, S. (2006). Dynamic data assimilation: a least
437 squares approach. Cambridge University Press

- 438 Metropolis, N., Rosenbluth, A. W., Rosenbluth, M. N., Teller, A. H., & Teller, E. (1953).
439 Equation of state calculations by fast computing machines. *Journal of Chemical Physics*,
440 21(6), 1087–1092. <https://doi.org/10.1063/1.1699114>
- 441 Mitsui, N., Hori, T., Miyazaki, S., & Nakamura, K. (2010). Constraining interplate frictional
442 parameters by using limited terms of synthetic observation data for afterslip: a
443 preliminary test of data assimilation. *Theoretical and Applied Mechanics Japan*, 58, 113–
444 120. <https://doi.org/10.11345/nctam.58.113>
- 445 Miyazaki, S., & Heki, K. (2001). Crustal velocity field of southwest Japan. *Journal of*
446 *Geophysical Research*, 106(B3), 4305–4326. <https://doi.org/10.1029/2000JB900312>
- 447 Okada, Y. (1992). Internal deformation due to shear and tensile faults in a half-space. *Bull.*
448 *Seismol. Soc. Am.*, 82, 1018–1040.
- 449 Ozawa, S., Yarai, H., Imakiire, T., & Tobita, M. (2013). Spatial and temporal evolution of the
450 long-term slow slip in the Bungo Channel, Japan. *Earth, Planets, and Space*, 65(2), 67–
451 73. <https://doi.org/10.5047/eps.2012.06.009>
- 452 Press, W. H., Teukolsky, S. A., Vetterling, W. T., & Flannery, B. P. (1996). Numerical
453 recipes in Fortran 90 the art of parallel scientific computing. Cambridge university press.
- 454 Radiguet, M., Perfettini, H., Cotte, N. et al. (2016). Triggering of the 2014 M_w 7.3 Papanoa
455 earthquake by a slow slip event in Guerrero, Mexico. *Nature Geosciences*, 9, 829–833.
456 <https://doi.org/10.1038/ngeo2817>
- 457 Rice, J. R. (1993). Spatio-temporal complexity of slip on a fault. *Journal of Geophysical*
458 *Research: Solid Earth*, 98(B6), 9885–9907. <https://doi.org/10.1029/93JB00191>
- 459 Ruina, A. (1983). Slip instability and state variable friction laws. *Journal of Geophysical*
460 *Research*, 88(B12), 10,359–10,370. <https://doi.org/10.1029/JB088iB12p10359>
- 461 Ruiz, S., Metois, M., Fuenzalida, A., Ruiz, J., Leyton, F., Grandin, R., Vigny, C., Madariaga,
462 R., & Campos, J. (2014). Intense foreshocks and a slow slip event preceded the 2014

- 463 Iquique M_w 8.1 earthquake. *Science*, 345, 1165–1169.
464 <https://doi.org/10.1126/science.1256074>
- 465 Seshimo, Y., & Yoshioka, S. (2022). Spatiotemporal slip distributions associated with the
466 2018–2019 Bungo Channel long-term slow slip event inverted from GNSS data. *Scientific*
467 *Reports*, 12(1), 343. <https://doi.org/10.1038/s41598-021-03982-6>
- 468 van Dinther, Y., Künsch, H. R., & Fichtner, A. (2019). Ensemble data assimilation for
469 earthquake sequences: Probabilistic estimation and forecasting of fault stresses.
470 *Geophysical Journal International*, 217(3), 1453–1478.
471 <https://doi.org/10.1093/gji/ggz063>
- 472 Voss, N., Dixon, T. H., Liu, Z., Malservisi, R., Protti, M., & Schwartz, S. (2018). Do slow
473 slip events trigger large and great megathrust earthquakes?. *Science advances*, 4(10),
474 eaat8472. <https://doi.org/10.1126/sciadv.aat8472>
- 475 Wessel, P., Smith, W. H., Scharroo, R., Luis, J., & Wobbe, F. (2013). Generic mapping tools:
476 improved version released. *Eos, Transactions American Geophysical Union*, 94(45), 409–
477 410.
- 478 Yoshioka, S., Matsuoka, Y., & Ide, S. (2015). Spatiotemporal slip distributions of three long-
479 term slow slip events beneath the Bungo Channel, southwest Japan, inferred from
480 inversion analyses of GPS data. *Geophysical Journal International*, 201(3), 1437–1455.
481 <https://doi.org/10.1093/gji/ggv022>